Published in final edited form as:
Nat Phys. 2014 September 1; 10(9): 676–682. doi:10.1038/nphys3017.

Quantum Coherence in Photosynthesis for Efficient Solar Energy Conversion

Elisabet Romero[1,*], **Ramunas Augulis**[2,†], **Vladimir I. Novoderezhkin**[3], **Marco Ferretti**[1], **Jos Thieme**[1,‡], **Donatas Zigmantas**[2], and **Rienk van Grondelle**[1]

[1]Department of Physics and Astronomy, VU University, Amsterdam, The Netherlands
[2]Department of Chemical Physics, Lund University, Lund, Sweden [3]A. N. Belozersky Institute of Physico-Chemical Biology, Moscow State University, Moscow, Russia

Abstract

The crucial step in the conversion of solar to chemical energy in Photosynthesis takes place in the reaction center where the absorbed excitation energy is converted into a stable charge separated state by ultrafast electron transfer events. However, the fundamental mechanism responsible for the near unity quantum efficiency of this process is unknown. Here we elucidate the role of coherence in determining the efficiency of charge separation in the plant photosystem II reaction centre (PSII RC) by comprehensively combining experiment (two-dimensional electronic spectroscopy) and theory (Redfield theory). We reveal the presence of electronic coherence between excitons as well as between exciton and charge transfer states which we argue to be maintained by vibrational modes. Furthermore, we present evidence for the strong correlation between the degree of electronic coherence and efficient and ultrafast charge separation. We propose that this coherent mechanism will inspire the development of new energy technologies.

Photosynthesis, the biological process whereby solar energy is stored as a fuel, is the vital link between the energy of the sun and life on earth. The highly efficient solar energy collection, transfer and conversion in photosynthesis is accomplished by specialized membrane-bound pigment-protein complexes. During the early steps of photosynthesis, light-harvesting (LH) complexes absorb and transfer solar excitation energy to the reaction center (RC), the site of energy conversion. In the RC the excitation energy is converted into a trans-membrane electrochemical potential with near unity quantum efficiency, i.e., almost each absorbed photon is converted into a charge separated state. Despite the current

[*]Contact information: Dr. Elisabet Romero, eli@few.vu.nl, Phone +31 20 5987426, Fax +31 20 5987999.
[†]Current address: Center for Physical Sciences and Technology, Vilnius, Lithuania
[‡]Current address: TU Delft, Applied Sciences ChemE/Chemical Engineering, Delft, The Netherlands

Author Contributions: E.R., R.A., M.F., J.T., and D.Z. collected the experimental 2DES data. R.A., and M.F. developed the data analysis programs. E.R analyzed the experimental data. V.I.N., E.R., and R.v.G. developed the theoretical modeling. E.R. D.Z., and R.v.G. designed the research. E.R., V.I.N., D.Z., and R.v.G. wrote the paper. All authors discussed the results and commented on the manuscript.

Competing financial interests: The authors declare no competing financial interests.

Europe PMC Funders Author Manuscripts

knowledge about the pathways and timescales of charge separation[1], the precise mechanism responsible for the high efficiency of this process is unknown.

In the 90's, the remarkable direct visualization of coherent nuclear motion in the excited state of the primary electron donor in the bacterial RC[2] (a simpler version of the PSII RC) suggested a functional role for these motions in the primary electron transfer reaction, a view later supported by theoretical models[3-4]. However, at that time, no coherence could be observed between the reactant and the product of that reaction. More recently, the observation of long-lived coherence in photosynthetic complexes (light-harvesting[5-12] and oxidized bacterial RC unable to perform charge separation[13-14]) has triggered an intense debate on the role of quantum coherence in promoting the efficiency of photosynthesis. Yet no clear correlation between coherence and efficiency of energy or electron transfer has been presented to date. In this context, quantum coherence between the electronic states involved in energy or electron transfer introduces correlations between the wavefunctions of these states[15] enabling the excitation to move rapidly and to coherently sample multiple pathways in space[16]. Therefore, the quantum coherence effect may render the process of energy and electron transfer less sensitive to the intrinsic disorder of pigment-protein complexes and allow these systems to successfully reach their final state avoiding energy losses.

Therefore, here we investigate two key questions: is electronic coherence present in the PSII RC? And in case it is, does coherence promote the PSII RC charge separation efficiency? To address these questions we apply two-dimensional electronic spectroscopy (2DES)[17] to the fully functional PSII RC.

The PSII RC complex contains six chlorophylls (Chl), two pheophytins (Phe), and two β-carotenes associated to the D_1/D_2 proteins. The central cofactors [four Chls and two Phes (P_{D1}, P_{D2}, Chl_{D1}, Chl_{D2}, Phe_{D1}, Phe_{D2})] (Fig. 1a) arranged in two quasi-symmetric branches[18-20], are involved in charge separation which proceeds selectively along the D_1 branch[21-22]. Upon excitation, the energy is delocalized among these cofactors leading to collective excited states (excitons, i.e., bound electron-hole pairs or Frenkel excitons[23]) mixed with charge transfer states (CT, i.e., separated and localized electron and hole). This mixing leads to excitons with CT character (exciton-CT, i.e., the excitons display a non-uniform electron density)[24] providing ultrafast channels for exciton relaxation and charge transfer. However, the RC has to cope with a counter effect: energetic disorder. Fast nuclear motions (intra- and inter-pigment and protein vibrations), give rise to dynamic disorder; while slow protein motions constitute static disorder. The disorder determines the energy landscape, it modulates the energy of the electronic states and determines the electronic configuration that initiates charge separation. Due to multiple protein conformations within the sample ensemble, unproductive conformations may appear leading to energy losses. One solution is the capacity to start charge separation from different protein conformations[25]. Indeed, we discovered that three exciton-CT states initiate charge separation: $(Chl_{D1}{}^{\delta+}Phe_{D1}{}^{\delta-})^*_{681nm}$ and $(P_{D2}{}^{\delta+}P_{D1}{}^{\delta-}Chl_{D1})^*_{673nm}$ /$(P_{D2}{}^{+}P_{D1}{}^{-})^{\delta}*_{684nm}$, via the so-called Chl_{D1} and P_{D1} pathways, respectively[24] (the subscripts indicate the central absorption wavelength while the superscripts $\delta+/\delta-$ and $\delta*$ indicate CT and exciton character, respectively). Since the participation of Chl_{D1} in $(P_{D2}{}^{\delta+}P_{D1}{}^{\delta-}Chl_{D1})^*_{673nm}$ is small, in the

following we refer to $(P_{D2}^{\delta+}P_{D1}^{\delta-})^*_{673nm}$ (note that this exciton-CT state has a high $(P_{D2}P_{D1})_+^*{}_{660nm}$ and a low $(P_{D2}^{\delta+}P_{D1}^{\delta-})^*_{673nm}$ energy component) (Fig. 1a).

Here, we comprehensively combine experimental (2DES) and theoretical (standard Redfield theory) methods to demonstrate that electronic-vibrational (vibronic) coherences are present in the PSII RC and that these coherences strongly correlate with efficient and ultrafast charge separation.

Two-dimensional electronic spectra

2DES reveals the presence of coherent effects in photosynthetic complexes utilizing three ultrashort and spectrally broad laser pulses separated by controlled time delays (Fig. 1b and Supplementary Fig. 1). Fourier transform with respect to the coherence time τ (time between the first and second pulses) and with respect to the rephasing time t (time between the third pulse and the signal) yields the 2D electronic spectrum in the frequency domain which correlates the absorption, ω_τ, and emission, ω_t, frequencies for a fixed population time T (time between the second and third pulses). The broad-band excitation (Fig. 1b) creates coherent superpositions of electronic/vibrational states giving rise to specific features in the 2D spectra.

Originally, below diagonal cross-peaks oscillating as a function of T were assigned to electronic coherences between excitons. Within that interpretation, the vibrational coherences modulated the diagonal amplitude[26] while energy transfer appeared as non-oscillating cross-peaks. More recently, electronic-vibrational (vibronic) models, with both diagonal and off-diagonal contributions, have been proposed based on specific vibrational modes resonant with the excitonic manifold energy gaps[27-32] (with a focus on energy transfer efficiency[29-30], on the role of non-equilibrium vibrations[27,31] and on the role of ground-state vibrational coherence[32]) as well as models based on displaced potential energy surfaces[33]. In reference[31] the authors show that the resonant electronic-vibrational configuration sustains, regenerates, or even creates coherence between electronic states during the time scale of energy and electron transfer. This mechanism does not require coherent laser excitation, it is also valid for incoherent sunlight excitation[31,34]. In 2DES, the laser excitation is a tool that allows to visualize and study coherence in photosynthesis.

We measured the 2D spectra of the PSII RC at room (277 K or RT) and cryogenic (80 K) temperature. The RT dataset is more representative of the *in vivo* conditions while the 80 K dataset has an enhanced spectral resolution. Therefore, we compare both datasets to check for consistency (Supplementary Fig. 2-8) and use the 80 K dataset to interpret the 2D data. In all the PSII RC 2D spectra (Fig. 1c, Fig. 2a and Supplementary Fig. 2), an elongated feature red-shifted by 1 nm with respect to the diagonal corresponds to the bleach of: initially populated exciton-CT states ($0 \leq T \leq 1$ ps), charge-separated states ($T > 1$ ps), and $Chls_Z$ ($0 \leq T \leq 20$ ps). Two cross-peaks at $(\lambda_\tau, \lambda_t) \approx$ (645-660,665) and (655-670,675) nm are clearly present at early T ($0 \leq T \leq 60$ fs) revealing coherences between exciton-CT states. The (655-670,675) nm cross-peak increases in amplitude due to exciton relaxation (first hundreds of fs), energy transfer between exciton-CT (first ps), and energy transfer from the peripheral $Chls_Z$ to the central cofactors (20 ps). Note that these processes overlap in time

due to disorder. The 2D spectral evolution is consistent with a previous transient absorption study[25].

Quantum beats: oscillation frequencies

Quantum beats, amplitude oscillations as a function of *T*, are clearly present for, at least, 1 ps in the real rephasing 2D spectral traces (Fig. 1c) at both RT and 80 K. The traces are superimposed onto the multi-exponential decay or rise of the 2D spectral features, hence, a fitted two-exponential decay curve is subtracted from each trace prior to Fourier transform with respect to *T*, which allows to retrieve the oscillation frequencies. The observed frequencies (± 20 cm^{-1}) are: 100, 190, 240, 345, 390, and 740 cm^{-1} (RT) and 120, 190, 265, 340, 390, and 730 cm^{-1} (80 K) (Supplementary Fig. 3). Additionally, a group of frequencies is found only at 80 K: 440, 580, 610, 680, and 810 cm^{-1}. All these frequencies are present in the fluorescence line-narrowing (FLN) spectra of PSII RC[35] and monomeric Chl *a* in solution[36] indicating that they correspond to Chl *a* intra-molecular vibrations (Supplementary Table 1). Remarkably, these frequencies are in the range to optimally match energy differences between exciton-CT states in the PSII RC (Fig. 1a).

Quantum coherence and 2D frequency maps

The amplitude distribution of each frequency in the 2D spectra is represented in 2D frequency maps (Fig. 1d-g and Supplementary Fig. 4-9). The 2D frequency maps only show the states which oscillate at a specific frequency, i.e., the states which are coherent; where the coherence between different states is visualized as cross-peaks connecting these states. As a result, the 2D frequency map representation provides higher selectivity than the 2D spectra since the latter contains the spectral features of all the exciton-CT states while the former displays only the coherent states. This method presents a clear advantage with respect to the commonly used 2D trace representation because it allows to directly visualize the coherence between all the states in the system in a single 2D frequency map[37]. Recently this method has been employed to investigate the nature of the coherences in a bacteriochlorophyll dimer[38]. In that model system, the Fourier transform analysis and the modeling of the spectral responses in a complete basis of electronic and vibrational states shows the 2D frequency maps amplitude distribution for mixed electronic-vibrational (vibronic) coherences: the frequencies with predominant electronic coherence contribution appear mainly as cross-peaks while in the frequency maps with large vibrational contribution the diagonal amplitude distribution dominates. Thus, according to their amplitude distribution, the frequencies can be divided into two groups: with and without off-diagonal contribution, that is: i) 120 and 265 cm^{-1} (cross-peaks) and 190, 340, 390, and 730 cm^{-1} (diagonal and cross-peaks, observed at both RT and 80 K) and ii) 440, 580, 610, 680, and 810 cm^{-1} (diagonal, present only at 80 K). In the following we analyze the 2D frequency maps for some representative frequencies based on the known energies of the exciton-CT absorption bands[24] (Table 1) (for the analysis of all frequencies see Supplementary Table 1 and Fig. 4-9, for a detailed coherent energy levels scheme see Supplementary Fig. 10).

Europe PMC Funders Author Manuscripts

120 ± 20 cm^{-1}

This frequency is distributed along a line parallel and red-shifted 130 cm^{-1} with respect to the diagonal (Fig. 1d) with maximum amplitude at ($\lambda_\tau \lambda_t$) equal to (675-676.5,681-682.5) nm corresponding to the ($P_{D2}^{\delta+}P_{D1}^{\delta-}$)$_-$*$_{675\text{-}676.5nm}$ and ($Chl_{D1}^{\delta+}Phe_{D1}^{\delta-}$)*$_{681\text{-}682.5nm}$ exciton-CT states, respectively. This elongated cross-peak indicates that ($P_{D2}^{\delta+}P_{D1}^{\delta-}$)$_-$*$_{675\text{-}676.5nm}$ and ($Chl_{D1}^{\delta+}Phe_{D1}^{\delta-}$)*$_{681\text{-}682.5nm}$ oscillate at the same frequency, i.e., these excitons are coherent. The resonance between the beating frequency and the exciton energy gap points to the coupling of a 120 cm^{-1} Chl *a* intra-molecular vibrational mode to these states. However, the distribution of this beating frequency mainly as a cross-peak indicates that predominantly electronic coherence is observed between these two exciton states. Considering that these states initiate charge separation via the P_{D1} and Chl_{D1} pathways, respectively, and that coherence enables directed wave-like energy transfer between states (as it has been previously suggested by theory[39]), we propose that this coherence allows the sampling of the energy landscape (or switching between pathways) until the system finds the optimal route towards charge separation.

440 ± 20 cm^{-1}

This frequency is distributed on the diagonal (Fig. 1e) indicating that this vibrational mode modulates the amplitude of a population, most likely the ($Chl_{D1}^{\delta+}Phe_{D1}^{\delta-}$)*$_{681nm}$ state. It is interesting to note that similar diagonal distribution corresponding to mostly vibrational coherence is observed for all frequencies present only at 80 K (Supplementary Fig. 9).

340 (730) ± 20 cm^{-1}

The 340 and 730 cm^{-1} 2D frequency maps are similar (Fig. 1f-g) with the amplitude distributed near the diagonal and in cross-peaks along three lines parallel to the diagonal: at ≈315 (730) cm^{-1}, at ≈610 (1500) cm^{-1} (below diagonal), and ≈380 (685) cm^{-1} (above diagonal). This indicates that both frequencies correspond to mixed electronic-vibrational coherence. These frequencies match the span of energy differences between ($P_{D2}P_{D1}$)$_+$*$_{\approx 665(646)nm}$ and ($P_{D2}^{\delta+}P_{D1}^{\delta-}$)$_-$*$_{\approx 678(681)nm}$, and between ($P_{D2}^{\delta+}P_{D1}^{\delta-}$)$_-$*$_{\approx 678(675)nm}$ and ($P_{D2}^{\delta+}P_{D1}^{\delta-}$)$^{\delta*}_{\approx 690(710)nm}$ (Fig. 1a and Table 1), thus these 2D maps show the resonant coupling of the 340 (730) cm^{-1} vibrational mode to the exciton-CT states contributing to the P_{D1} charge separation pathway. The coherence between exciton and CT state (with CT and exciton character, respectively) allows coherent electron transfer which implies that charge separation in the PSII RC proceeds via a coherent mechanism.

All these observations demonstrate that in the PSII RC long-lived coherences observed at physiological temperature (RT) have vibronic origin and that these coherences persist on the timescale of charge separation. Furthermore, the amplitude of the quantum beats with respect to the total signal amplitude for the cross-peaks discussed above (Fig 1c), indicates that a large fraction of the RCs within the sample ensemble display coherence. Therefore, we propose that vibronic coherence make essential contributions to the ultimate high quantum efficiency.

Redfield model: 2D spectra

To explain the energy conversion dynamics in the PSII RC, i.e., the 2D spectral shape and time evolution, we apply our *disordered exciton-CT* model[40-41] [for a detailed description of the model (Hamiltonian, model of disorder, spectral density, dynamic equations for coherent evolution) see Supplementary Equations and Tables 2-4]. In the model, the excited-state manifold consists of the electronic excited state of all chlorines (Chl and Phe) and four CT states. The site energies of the cofactors were determined from a simultaneous and quantitative fit of eight steady-state spectra[40] using the modified Redfield approach with a realistic spectral density (extracted from the fluorescence line-narrowing spectrum[35]). The origin of the primary CT state (strongly mixed with the cofactors excited states) was assigned to $P_{D2}^{+}P_{D1}^{-}$ by modeling the Stark spectrum. Parameters of the secondary [($P_{D1}^{+}Chl_{D1}^{-}$) and ($Chl_{D1}^{+}Phe_{D1}^{-}$)] and final ($P_{D1}^{+}Phe_{D1}^{-}$) CT states have been determined from the modeling of the transient absorption kinetics[41].

To investigate the coherences between electronic states, we switch from modified to standard Redfield theory with the full relaxation tensor which includes the dynamics of the electronic coherences and the nonsecular population-to-coherence transfers (but does not include vibronic contributions). The formation of the secondary and final CT states from the excited states (mixed with $P_{D2}^{+}P_{D1}^{-}$) are calculated using generalized Förster theory[41]. The parameters are the same as used previously[41]. This approach allows an excellent fit of the 2D spectral features and dynamics (Fig. 2). The comparison of the experimental and calculated 2D spectra at four representative *T* shows an overall agreement for all (including off-diagonal) spectral features. Nevertheless, two discrepancies are found: i) the anti-diagonal width of the elongated diagonal feature is broader, and ii) the diagonal bleach at 670 nm is less pronounced. The first discrepancy is due to Lorentzian wings which describe the homogeneous broadening in standard Redfield theory. Regarding the second discrepancy, the diagonal distribution is given by a combination of the cofactors bleach and their electrochromic shifts induced by the CT states. Although these features are included in the model, it remains difficult to reproduce all details of the observed 2D spectra.

In a recent publication[42], our *2007* model[40] (with only one CT state) was used to calculate the previously obtained PSII RC 2D spectra[43]. A detailed comparison between that work and our approach is given in the Supplementary Discussion.

Redfield model: specific realizations

The *disordered exciton-CT* model is used to generate the dynamics of the site populations of the cofactors excited states and the primary CT state for specific realizations of the disorder in order to investigate the effect of coherence on charge separation. Here, we generate different realizations *in silico* in the same way as the protein does *in vivo*, by varying the energy gap between the cofactors site energies. In this representation, coherence is seen as anticorrelated oscillations in the site populations of the coupled cofactors and the role of coherence is determined by the speed and efficiency of the $P_{D2}^{+}P_{D1}^{-}$ CT state formation.

The dynamics of the site populations averaged over disorder along with the dynamics for two specific disorder realizations are shown in Fig. 3 (more realizations are shown in

Supplementary Fig. 11). In the realization displayed in Fig. 3b, P_{D1} and P_{D2} are strongly coupled to the $P_{D2}^{+}P_{D1}^{-}$ CT state as indicated by the anticorrelated oscillations between P_{D1}/P_{D2} and $P_{D2}^{+}P_{D1}^{-}$ during the first 250 fs. This produces ultrafast, 50 fs, and efficient population of the $P_{D2}^{+}P_{D1}^{-}$ state via exciton relaxation from the P_{D1} and P_{D2} excited states. For other realizations with weaker coherence between P_{D1}/P_{D2} and $P_{D2}^{+}P_{D1}^{-}$, the formation of $P_{D2}^{+}P_{D1}^{-}$ is slower and less efficient (Supplementary Fig. 11). These dynamics illustrate the solid correlation between electronic coherence and ultrafast and efficient electron transfer via the P_{D1} path. In the realization shown in Fig. 3c, Chl_{D1} is coherently coupled with P_{D2} and Phe_{D1} as indicated by their anticorrelated oscillations. Such coupling produces effective energy flow from P_{D2} to Chl_{D1} seen as the P_{D2} decay and the Chl_{D1} rise within 50 fs. At 300 fs, Chl_{D1} and Phe_{D1} decay due to the formation of $Chl_{D1}^{+}Phe_{D1}^{-}$. In this realization charge separation does not proceed via $P_{D2}^{+}P_{D1}^{-}$ and therefore, the formation of this CT state is slow and inefficient. The dynamics of the Chl_{D1} and Phe_{D1} population indicate that this realization follows the Chl_{D1} path.

The calculated population dynamics demonstrates that the efficiency of energy and electron transfer in the PSII RC strongly correlates with the degree of electronic coherence between the excited and primary CT states, the stronger the coherence, the faster and more efficient the process is. The direction and speed of energy transfer is related to the degree of electronic coherence between the excited states of the cofactors, i.e., the coherence between cofactors produces ultrafast energy transfer along a *wired* molecular chain[39]. We show that the coherence between exciton and CT states results in ultrafast and efficient charge separation. Therefore we conclude that the correlation between electronic coherence and the speed and efficiency of charge separation strongly supports the idea that electronic coherence plays a major role in determining the speed and efficiency of the first charge separation step.

The role of Quantum coherence

The combination of experimental and theoretical evidence presented in the previous sections provides a link between the presence of quantum coherence and its biological functional role in the PSII RC.

According to the *disordered exciton-CT* model, which captures the 2D spectral shape and overall time evolution very well, in the specific realizations shown in Fig. 3b-c the coherence decays in around 400 fs. In the averaged over disorder picture (Fig. 3a), analogous to the measured kinetics, the coherences appear much weaker and decay in about 300 fs due to disorder induced dephasing as a result of ensemble averaging. However, the experimental 2D traces show up to 1 ps long-lived oscillations (Fig. 1c). The most obvious reason for this discrepancy is the fact that our model developed in a pure exciton basis does not include the effects of coupled exciton-vibrational dynamics (generally containing a non-trivial interplay of electronic and vibrational coherences)[38] which has been proposed as a possible origin for long-lived oscillations[27-32].

The mechanism in which long-lived electronic coherences are sustained by non-equilibrium vibrational modes is strongly supported by two additional facts: i) the dominant 2DES

frequencies observed at both RT and 80 K (120, 190, 265, 340, 390, and 730 cm^{-1}) correspond to Chl *a* vibrational modes that match the energy gaps between the exciton-CT states which initiate charge separation[24], and ii) the 2D frequency maps show that the oscillating electronic states are the ones involved in each specific exciton-CT energy gap. Therefore, we conclude that vibration-assisted electronic (vibronic) coherence is present in the PSII RC and, as indicated by the relative quantum beats amplitude, it exists in a large fraction of PSII RCs. Furthermore, the correlation between electronic coherence and efficiency indicates that vibronic coherence is utilized by the system to drive ultrafast and efficient charge separation. Therefore, in line with recent theoretical work[27-32], we have shown that vibronic coherences survive the aggressive background noise and consequently may play an essential role on charge separation dynamics.

Based on the substantial evidence presented, we propose that the PSII RC has evolved a delicately tuned and robust environment to provide the required exciton-vibrational matching for efficient solar energy conversion and, consequently, that the plant PSII RC operates as a *quantum designed light trap*[44].

Methods

Sample preparation

The PSII RC (D_1-D_2-cyt b_{559}) complexes were isolated from spinach as described previously[45]. For the 80 K experiments the sample was diluted in a buffer containing 60 % glycerol (v/v), 20 mM BisTris pH 6.5 and 0.06 % β-DM to an optical density of ≈ 0.2 in 200 μm at 678 nm. For the 277 K experiments the sample was diluted in a buffer containing 10 % glycerol (v/v), 20 mM BisTris pH 6.5 and 0.03 % β-DM to an optical density of ≈ 0.2 in 500 μm at 675 nm. The RT sample was circulated via a flow cell pumped by a peristaltic pump.

Experimental setup and data acquisition

2D electronic spectra were measured with a diffractive optic-based inherently phase-stabilized four-wave mixing setup[46-47] using double modulation lock-in detection for additional noise reduction and sensitivity enhancement[48]. The laser system (PHAROS, Light Conversion) repetition rate was 500 Hz and 2 kHz for the 80 K and 277 K experiments, respectively. The laser pulses generated by a home-built NOPA and compressor were centered at 680 nm (80 nm full-width at half-maximum) and had a pulse duration of 16 fs. During the experiment, four pulses (three with 5 nJ per pulse and a local oscillator attenuated by three orders of magnitude) were focused on the sample to a spot size of 100 μm. The coherence time (τ) was scanned in 1 fs steps from −170 to 400 fs and from −110 to 130 fs for the 80 and 277 K experiments, respectively. The population time (T) was scanned with 20 fs steps from 0 to 1 ps. Additionally, 2D spectra at longer T (−1, 2, 5, 10, 20 and 50 ps) were recorded.

Supplementary Material

Refer to Web version on PubMed Central for supplementary material.

Acknowledgements

We thank H. van Roon for preparation of the PSII RC sample. E. R., M. F., J. T. and R. v. G. were supported by the VU University Amsterdam, the Laserlab-Europe Consortium, the TOP grant (700.58.305) from the Foundation of Chemical Sciences part of NOW and the advanced investigator grant (267333, PHOTPROT) from the European Research Council. E. R., M. F. and R. v. G. were supported by the EU FP7 project PAPETS (GA 323901). V. I. N. was supported by Russian Foundation for Basic Research (grant No. 12-04-01085) and by a NWO visitor grant. Work in the laboratory of D. Z. was supported by the Swedish Research Council, Knut and Alice Wallenberg Foundation and Wenner-Gren Foundations.

References

1. Blankenship, RE. Molecular Mechanisms Of Photosynthesis. Blackwell Science Ltd; Oxford: 2002.
2. Vos MH, Rappaport F, Lambry J-C, Breton J, Martin J-L. Visualization of coherent nuclear motion in a membrane protein by femtosecond spectroscopy. Nature. 1993; 363:320–325.
3. Parson WW, Warshel A. A density-matrix model of photosynthetic electron transfer with microscopically estimated vibrational relaxation times. Chem. Phys. 2004; 296:201–216.
4. Novoderezhkin VI, Yakovlev AG, Van Grondelle R, Shuvalov VA. Coherent nuclear and electronic dynamics in primary charge separation in photosynthetic reaction centers: A Redfield theory approach. J. Phys. Chem. B. 2004; 108:7445–7457.
5. Savikhin S, Buck DR, Struve WS. Oscillating anisotropies in a bacteriochlorophyll protein: Evidence for quantum beating between exciton levels. Chemical Physics. 1997; 223:303–312.
6. Brixner T, et al. Two-dimensional spectroscopy of electronic couplings in photosynthesis. Nature. 2005; 434:625–628. [PubMed: 15800619]
7. Zigmantas D, et al. Two-dimensional electronic spectroscopy of the B800-B820 light-harvesting complex. Proc. Natl. Acad. Sci. U. S. A. 2006; 103:12672–12677. [PubMed: 16912117]
8. Engel GS, et al. Evidence for wavelike energy transfer through quantum coherence in photosynthetic systems. Nature. 2007; 446:782–786. [PubMed: 17429397]
9. Calhoun TR, et al. Quantum coherence enabled determination of the energy landscape in light-harvesting complex II. J. Phys. Chem. B Lett. 2009; 113:16291–16295.
10. Collini E, et al. Coherently wired light-harvesting in photosynthetic marine algae at ambient temperature. Nature. 2010; 463:644–647. [PubMed: 20130647]
11. Schlau-Cohen GS, et al. Elucidation of the timescales and origins of quantum electronic coherence in LHCII. Nat. Chem. 2012; 4:389–395. [PubMed: 22522259]
12. Hildner R, Brinks D, Nieder JB, Cogdell RJ, van Hulst NF. Quantum coherent energy transfer over varying pathways in single light-harvesting complexes. Science. 2013; 340:1448–1451. [PubMed: 23788794]
13. Lee H, Cheng YC, Fleming GR. Coherence dynamics in photosynthesis: protein protection of excitonic coherence. Science. 2007; 316:1462–1465. [PubMed: 17556580]
14. Westenhoff S, Palecek D, Edlund P, Smith P, Zigmantas D. Coherent picosecond exciton dynamics in a photosynthetic reaction center. J. Am. Chem. Soc. 2012; 134:16484–16487. [PubMed: 23009768]
15. Scholes GD, Fleming GR, Olaya-Castro A, van Grondelle R. Lessons from nature about solar light harvesting. Nat. Chem. 2011; 3:763–774. [PubMed: 21941248]
16. Cheng YC, Fleming GR. Dynamics of light harvesting in photosynthesis. Annu. Rev. Phys. Chem. 2009; 60:241–262. [PubMed: 18999996]
17. Schlau-Cohen GS, Dawlaty JM, Fleming GR. Ultrafast multidimensional spectroscopy: Principles and applications to photosynthetic systems. IEEE J. Sel. Topics Quantum Electron. 2012; 18:283–295.
18. Ferreira KN, Iverson TM, Maghlaoui K, Barber J, Iwata S. Architecture of the photosynthetic oxygen-evolving center. Science. 2004; 303:1831–1838. [PubMed: 14764885]
19. Umena Y, Kawakami K, Shen J-R, Kamiya N. Crystal structure of oxygen-evolving photosystem II at a resolution of 1.9 Å. Nature. 2011; 473:55–60. [PubMed: 21499260]

20. Kern J, et al. Simultaneous femtosecond X-ray spectroscopy and diffraction of photosystem II at room temperature. Science. 2013; 340:491–495. [PubMed: 23413188]
21. Diner BA, Rappaport F. Structure, dynamics, and energetics of the primary photochemistry of photosystem II of oxygenic photosynthesis. Annu. Rev. Plant Biol. 2002; 53:551–580. [PubMed: 12221988]
22. Steffen MA, Lao K, Boxer SG. Dielectric asymmetry in the photosynthetic reaction center. Science. 1994; 264:810–816. [PubMed: 17794722]
23. Frenkel J. On the transformation of light into heat in solids. I. Phys. Rev. 1931; 37:17–44.
24. Romero E, et al. Mixed exciton-charge-transfer states in photosystem II: Stark spectroscopy on site-directed mutants. Biophys. J. 2012; 103:185–194. [PubMed: 22853895]
25. Romero E, van Stokkum IHM, Novoderezhkin VI, Dekker JP, van Grondelle R. Two different charge separation pathways in photosystem II. Biochemistry. 2010; 49:4300–4307. [PubMed: 20415453]
26. Cheng YC, Fleming GR. Coherence quantum beats in two-dimensional electronic spectroscopy. J. Phys. Chem. A. 2008; 112:4254–4260. [PubMed: 18376878]
27. Kolli A, Nazir A, Olaya-Castro A. Electronic excitation dynamics in multichromophoric systems described via a polaron-representation master equation. J. Chem. Phys. 2011; 135:154112. [PubMed: 22029302]
28. Christensson N, Kauffmann HF, Pullerits T, Mancal T. Origin of long-lived coherences in light-harvesting complexes. J. Phys. Chem. B. 2012; 116:7449–7454. [PubMed: 22642682]
29. Chin AW, Huelga SF, Plenio MB. Coherence and decoherence in biological systems: principles of noise-assisted transport and the origin of long-lived coherences. Phil. Trans. R. Soc. A. 2012; 370:3638–3657. [PubMed: 22753818]
30. Kolli A, O'Reilly EJ, Scholes GD, Olaya-Castro A. The fundamental role of quantized vibrations in coherent light harvesting by cryptophyte algae. J. Chem. Phys. 2012; 137:174109. [PubMed: 23145719]
31. Chin AW, et al. The role of non-equilibrium vibrational structures in electronic coherence and recoherence in pigment-protein complexes. Nat. Phys. 2013; 9:113–118.
32. Tiwari V, Peters WK, Jonas DM. Electronic resonance with anticorrelated pigment vibrations drives photosynthetic energy transfer outside the adiabatic framework. Proc. Natl. Acad. Sci. U. S. A. 2013; 110:1203–1208. [PubMed: 23267114]
33. Butkus V, Zigmantas D, Valkunas L, Abramavicius D. Vibrational vs. electronic coherences in 2D spectrum of molecular systems. Chem. Phys. Lett. 2012; 545:40–43.
34. Fassioli F, Olaya-Castro A, Scholes GD. Coherent energy transfer under incoherent light conditions. J. Phys. Chem. Lett. 2012; 3:3136–3142. [PubMed: 26296019]
35. Peterman EJG, van Amerongen H, van Grondelle R, Dekker JP. The nature of the excited state of the reaction center of photosystem II of green plants: A high-resolution fluorescence spectroscopy study. Proc. Natl. Acad. Sci. U.S.A. 1998; 95:6128–6133. [PubMed: 9600929]
36. Rätsep M, Linnanto J, Freiberg A. Mirror symmetry and vibrational structure in optical spectra of chlorophyll *a*. J. Chem. Phys. 2009; 130:194501. [PubMed: 19466837]
37. Milota F, et al. Vibronic and vibrational coherences in two-dimensional electronic spectra of supramolecular J-aggregates. J.Phys.Chem. A. 2013; 117:6007–6014. [PubMed: 23461650]
38. Ferretti M, et al. The nature of coherences in the B820 bacteriochlorophyll dimer revealed by two-dimensional electronic spectroscopy. Phys. Chem. Chem. Phys. 2013 doi:10.1039/c3cp54634a.
39. Ishizaki A, Fleming GR. Theoretical examination of quantum coherence in a photosynthetic system at physiological temperature. Proc. Natl. Acad. Sci. U. S. A. 2009; 106:17255–17260. [PubMed: 19815512]
40. Novoderezhkin VI, Dekker JP, van Grondelle R. Mixing of exciton and charge-transfer states in Photosystem II reaction centers: Modeling of Stark spectra with modified redfield theory. Biophys. J. 2007; 93:1293–1311. [PubMed: 17526589]
41. Novoderezhkin VI, Romero E, Dekker JP, van Grondelle R. Multiple charge separation pathways in photosystem II: modeling of transient absorption kinetics. ChemPhysChem. 2011; 12:681–688. [PubMed: 21322104]

42. Lewis KLM, et al. Simulations of the two-dimensional electronic spectroscopy of the photosystem II reaction center. J. Phys. Chem. A. 2013; 117:34–41. [PubMed: 23210463]
43. Myers JA, et al. Two-dimensional electronic spectroscopy of the D1-D2-cyt b559 photosystem II reaction center complex. J. Phys. Chem. Lett. 2010; 1:2774–2780.
44. van Grondelle R, Novoderezhkin VI. Quantum design for a light trap. Nature. 2010; 463:614–615. [PubMed: 20130637]
45. Kwa SLS, Newell WR, van Grondelle R, Dekker JP. The reaction center of photosystem II studied with polarized fluorescence spectroscopy. Biochim. Biophys. Acta. 1992; 1099:193–202.
46. Brixner T, Mancal T, Stiopkin IV, Fleming GR. Phase-stabilized two-dimensional electronic spectroscopy. J. Chem. Phys. 2004; 121:4221–4236. [PubMed: 15332970]
47. Brixner T, Stiopkin IV, Fleming GR. Tunable two-dimensional femtosecond spectroscopy. Opt. Lett. 2004; 29:884–886. [PubMed: 15119410]
48. Augulis R, Zigmantas D. Two-dimensional electronic spectroscopy with double modulation lock-in detection: enhancement of sensitivity and noise resistance. Opt. Express. 2011; 19:13126–13133. [PubMed: 21747465]

Europe PMC Funders Author Manuscripts

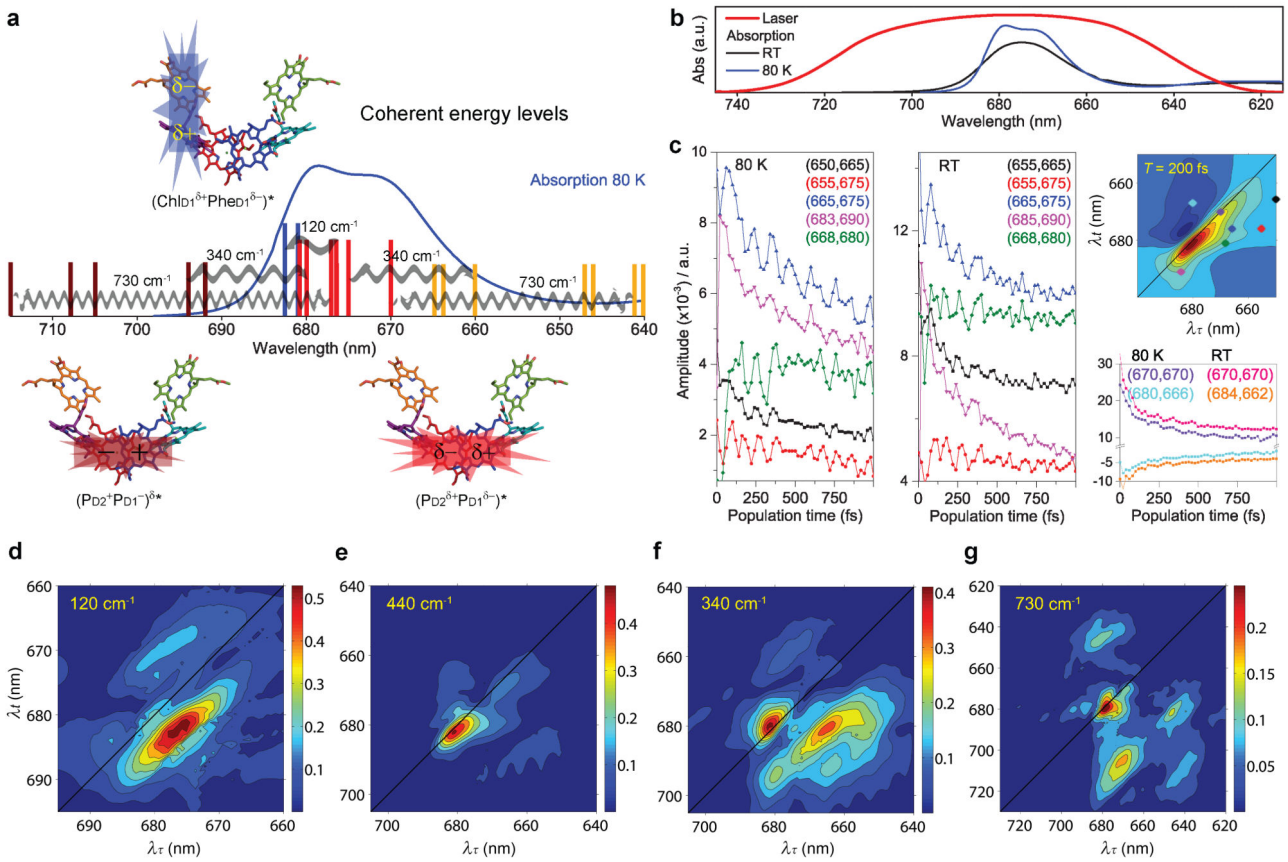

Fig. 1. The electronic structure of the PSII RC

(**a**) Exciton-CT states configuration and coherent energy levels scheme. The energy of the exciton-CT states in the different realizations of the disorder (central wavelength) is represented as vertical lines on top of the 80 K absorption spectrum. The spatial distribution of the exciton-CT states is shown on top of the X-ray crystal structure of the PSII RC (cofactor arrangement adapted from[19]): stars and rectangles represent exciton and CT character, respectively. Line colour code: $(P_{D2}P_{D1})_{+}{}^{*}{}_{660nm}$ (orange), $(P_{D2}{}^{\delta+}P_{D1}{}^{\delta-})_{-}{}^{*}{}_{673nm}$ (red), $(P_{D2}{}^{+}P_{D1}{}^{-})^{\delta*}{}_{684nm}$ (dark red) and $(Chl_{D1}{}^{\delta+}Phe_{D1}{}^{\delta-})^{*}{}_{681nm}$ (blue). Cofactors colour code: P_{D1} (red), P_{D2} (blue), Chl_{D1} (purple), Chl_{D2} (cyan), Phe_{D1} (orange) and Phe_{D2} (green). The horizontal wiggled arrows represent the coherences between electronic states observed as cross-peaks in the 120, 340 and 730 cm^{-1} 2D frequency maps (Fig. 1d,f-g and Table 1). (**b**) Absorption spectra and laser spectral profile. (**c**) Representative 2D spectral traces (left and central panel: cross peaks; bottom right panel: diagonal peaks) and their location in the real rephasing 2D spectrum at T = 200 fs (top right frame). Some traces have been translated vertically for better visualization. (**d-f**) 120, 440, 340 and 730 cm^{-1} 2D frequency maps.

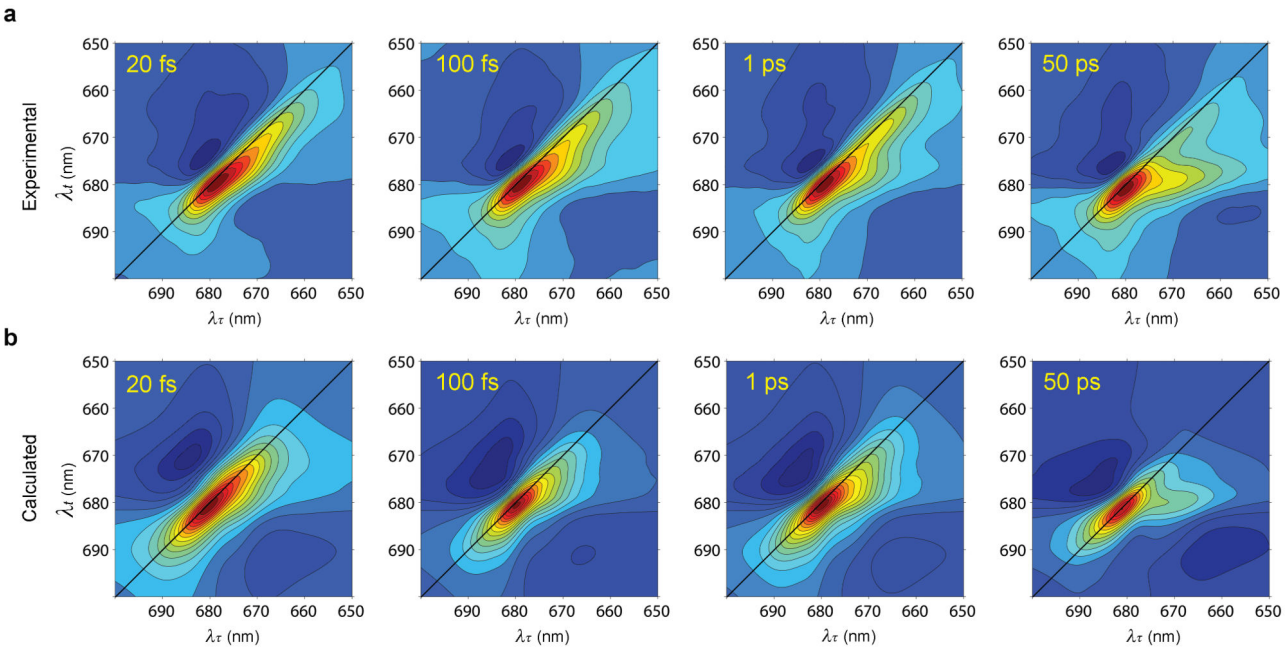

Fig. 2. Experimental vs. calculated real rephasing 2D PSII RC spectra at 80K

(**a**) Experimental PSII RC real rephasing 2D spectra at T = 20 fs, 100 fs, 1 ps and 50 ps. (**b**) Calculated PSII RC real rephasing 2D spectra at T = 20 fs, 100 fs, 1 ps and 50 ps. These 2D spectra are calculated with Standard Redfield theory according to the parameters of our *disordered exciton-CT* model[41] (Supplementary Equations and Tables 2-4).

Europe PMC Funders Author Manuscripts

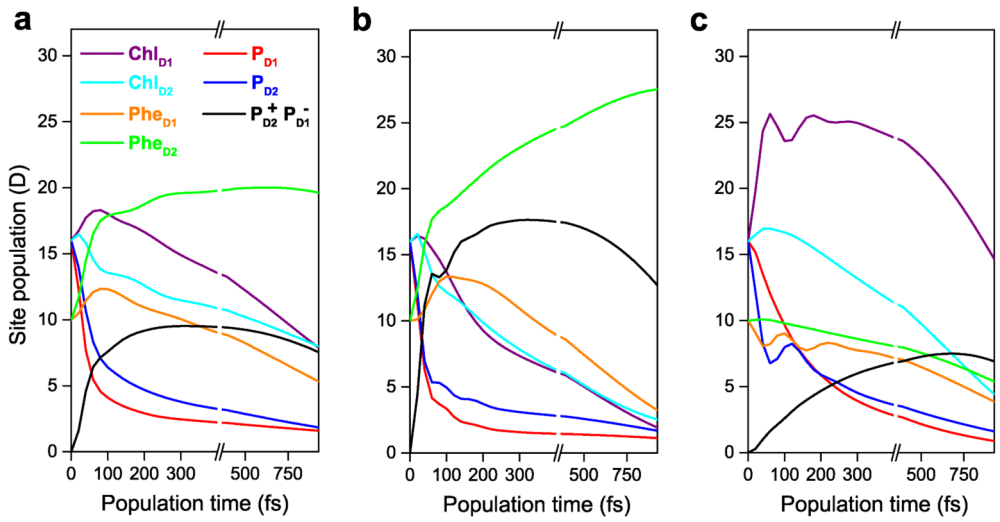

Fig. 3. Calculated dynamics of the site populations of the cofactors excited states and the primary CT state

(**a**) Dynamics averaged over all realizations of the disorder. (**b-c**) Dynamics corresponding to specific realizations of the disorder: (**b**) the P_{D1} charge separation pathway dominates. (**c**) the Chl_{D1} path dominates (note that the formation of the $Chl_{D1}^{+}Phe_{D1}^{-}$ is not shown in the figure). The legend is common for all panels. The scale is linear before the break and logarithmic after the break. The populations are created by the first two pulses with zero coherence time ($\tau = 0$). The initial site populations of the cofactors correspond to their transition dipole strength, 16 D for Chl and 10 D for Phe.

Europe PMC Funders Author Manuscripts

Table 1

Frequency distribution maxima for the 340 and 730 cm^{-1} 2D frequency maps

The centre of the frequency amplitude maxima corresponding to each exciton-CT state is displayed together with the difference in energy between the states contributing to each maxima observed in the 340 and 730 cm^{-1} 2D frequency maps. The values highlighted in bold correspond to the coherence wavelength, λ_c.

	$(P_{D2}^{\delta+}P_{D1}^{\delta-})_+$* nm	$P_{D2}^{\delta+}P_{D1}^{\delta-})_-$* nm	$(P_{D2}^{+}P_{D1}^{-})^{\delta}$* nm	$\Delta\omega$ cm^{-1}
340 cm^{-1}	**665**	680		330
	664		692	610
	660	**677**		380
		681,680		20
		680	694	300
730 cm^{-1}	**647**	681		770
	640		708	1500
	641	**670**		675
		669,671		45
		670	705	740
	646	**681**		795
		679,680		20
		680	715	720